



Contents lists available at ScienceDirect

## Materials Today: Proceedings

journal homepage: [www.elsevier.com/locate/matpr](http://www.elsevier.com/locate/matpr)

# Effect of laser power in laser powder bed fusion on Ni content and structure of Nitinol

E.M. Sequeda Leon<sup>a</sup>, S. Singamneni<sup>a</sup>, T. Guraya<sup>b</sup>, Z.W. Chen<sup>a,\*</sup>

<sup>a</sup> Department of Mechanical Engineering, Auckland University of Technology, Auckland, New Zealand

<sup>b</sup> Department of Mining & Metallurgical Engineering & Materials Science, University of the Basque Country UPV/EHU, Bilbao, Spain

## ARTICLE INFO

## Article history:

Available online xxxx

## Keywords:

Track morphology  
Melting mode  
Austenite  
Martensite

## ABSTRACT

Laser powder bed fusion (LPBF) additive manufacturing is capable of producing Nitinol stents of complex shapes, but a slight change of Ni content during LPBF can result in the stents not being suitable. Thus, there is a need to predict how laser power (P) and thus energy (E) affects the two important outcomes of Nitinol LPBF: defect level and Ni content. In this study, how Ni content may change during LPBF has been studied under two conditions: a sufficiently low P (thus E) but close to fully dense condition and a sufficiently high P that has caused keyhole pore formation. The loss of Ni has been found to be 0.36at% and 0.56at% for the sufficiently low and sufficiently high P conditions. Thus, 0.4–0.5at%Ni loss is expected for defect-free Nitinol LPBF. The morphological features of the melt pool affecting defect formation and relating to how P affects Ni loss will be discussed. With the significant loss of Ni due to LPBF, for the starting powder, which contains 50.5at%Ni and is fully austenitic, the LPBF as-built structure has remained mainly austenitic, but the samples also contain a small amount of martensite.

Copyright © 2023 Elsevier Ltd. All rights reserved.

Selection and peer-review under responsibility of the scientific committee of the 16th Global Congress on Manufacturing and Management 2022. This is an open access article under the CC BY-NC-ND license (<http://creativecommons.org/licenses/by-nc-nd/4.0/>).

## 1. Introduction

A major biomedical application of Nitinol (an equiatomic or near equiatomic NiTi alloy) is for stenting, which relies on the excellent superelasticity that the alloy can offer at body temperature (37 °C). Superelasticity results from austenite → martensite (A → M or B2 → B19') when the applied stress reaches a critical value, and the superelastic strain is released due to M → A when the applied stress is relieved. The temperature at which M → A in stress-free state Nitinol is complete is called austenite transformation temperature ( $A_f$ ). Ideally, for stenting,  $A_f$  should be less than 37 °C. However, the critical stress for A → M is lower for a higher  $A_f$ , thus selecting  $A_f$  is essential for designers of Nitinol stents, and in general,  $A_f$  should be close to 37 °C [1]. Frenzel et al. [2] conducted an extensive series of measurements using cast samples with at%Ni ranged from 44.0 to 51.2 and with the samples annealed at 950 °C for 24 h. Their study shows that, for at%Ni ≤ 50,  $A_f$  is stable at ~ 108 °C and  $A_f$  decreases sharply as Ni content increases slightly from 50at%Ni. For at%Ni = 50.7,  $A_f$  ≤ 37 °C.

Laser powder bed fusion (LPBF) is now a mature additive manufacturing technology after a period of intensive research on the process and on the structure and properties of LPBF parts [3], particularly after 2015 [4]. There is little restriction on the geometry of the parts and a thickness limit of LPBF has been demonstrated to be down to ~ 0.1 mm [5]. Thus, LPBF is potentially suited for making Nitinol devices. However, as the vaporization temperature of Ni (2730 °C) is significantly lower than that of Ti (3287 °C), Ni loss more than Ti loss can occur during LPBF. Thus, LPBF of Nitinol for stenting application is challenging as a slight variation from the desirable Ni content can cause an undesirable  $A_f$ . Reviewing the studies of Nitinol LPBF, Mohamed et al. [6] have shown that  $A_f$  increases as laser volumetric energy density (E) increases and linked this to, as commonly understood, more loss of Ni using higher E due to vaporization. The more detailed demonstration of how laser power (P) affects both Ni loss on one hand and affects the quality and structure of LPBF parts have, however, not been detailed.

It is well known that the formation of lack of fusion (LOF) and keyhole pore defects occurs during LPBF when operating conditions are outside the suitable conditions. Below the lower bound of the suitable E range, the lower the E, the higher the amount of LOF and above the upper bound of the suitable E range, the higher the E, the more keyhole pores form during LPBF. Thus, the knowl-

\* Corresponding author.

E-mail address: [zhan.chen@aut.ac.nz](mailto:zhan.chen@aut.ac.nz) (Z.W. Chen).

<https://doi.org/10.1016/j.matpr.2023.05.678>

2214-7853/Copyright © 2023 Elsevier Ltd. All rights reserved.

Selection and peer-review under responsibility of the scientific committee of the 16th Global Congress on Manufacturing and Management 2022.

This is an open access article under the CC BY-NC-ND license (<http://creativecommons.org/licenses/by-nc-nd/4.0/>).

edge of how much Ni loss may occur during Nitinol LPBF with the minimum level of defects is essential. In this present study, how LPBF in conditions close to the lower and upper bound E conditions may affect Ni loss have been studied. Evaluation of the morphological features of tracks to identify the modes of melting for the two conditions has been conducted and how the track features may affect the amount of Ni loss has been considered. Furthermore, structure analysis of samples has also been made to detect how Ni content change may affect the structure of the alloy after LPBF.

## 2. Materials and methods

LPBF experiments using Nitinol powder (15–53  $\mu\text{m}$  in size, from Hermus & OEM) were conducted using a Renishaw AM400 system, which is equipped with a 400 W ytterbium fibre laser operating in a pulsed laser mode with a wavelength of 1.070  $\mu\text{m}$  and a spot size of 70  $\mu\text{m}$ . A reduced-size attachment was used to conduct the experiment with a reduced amount of powder. During LPBF, a continuous flow of Ar was used. Two P values, 81 and 156 W, were used. Hatch distance and layer thickness were 64 and 40  $\mu\text{m}$ , respectively. Point distance was 50  $\mu\text{m}$ . The duration of the laser on time and off time within a laser pulse cycle were 50 and 10  $\mu\text{s}$ , respectively. Thus, corresponding to the two P values, the two E values were 44 and 85  $\text{J}/\text{mm}^3$ . Biffi et al. [7] have shown that by increasing E from 25 to  $\sim 50 \text{ J}/\text{mm}^3$  of Nitinol LPBF using Renishaw AM400, the relative density of samples increases rapidly to close to being fully dense. At 85  $\text{J}/\text{mm}^3$ , their data also suggest that LPBF samples have remained close to being fully dense. Thus, E = 44 and 85  $\text{J}/\text{mm}^3$  are suitable conditions to evaluate how much Ni loss may occur.

Built samples were sectioned parallel to build direction (BD) for metallography following the normal grinding and polishing procedure and for X-ray diffraction (XRD). Polished samples were etched using the Kroll's reagent: 87.7%  $\text{H}_2\text{O}$ , 14.1%  $\text{HNO}_3$ , and 3.2% HF for 30 s. Samples were examined using a Hitachi SU-70 scanning electron microscope (SEM) with energy-dispersive X-ray spectroscopy (EDS) capability. Ni contents of LPBF samples were determined using EDS, and, in order to more constantly estimate the change of Ni content after LPBF, Ni content of the as-received powder was also determined using EDS. Thus, the powder was also mounted and polished. For measuring the fraction of LOF ( $f_{\text{LOF}}$ ) and the fraction of keyhole pores ( $f_{\text{Pores}}$ ) on the metallography samples, 12 images were taken in each polished sample without etching and ImageJ software was used to estimate  $f_{\text{LOF}}$  and  $f_{\text{Pores}}$ . Diffraction experiments were performed using an X-ray diffractometer with monochromatized  $\text{CuK}\alpha_1$  radiation ( $\lambda = 0.154 \text{ nm}$ ). The scanning range ( $2\theta$ ) was from 20 to 80°. Data from the Joint Committee on Powder Diffraction Standards (JCPDS) [8] were used to identify the phases.

## 3. Results and discussion

### 3.1. Laser power/energy, defects and track morphological features

Fig. 1 shows the track features of LPBF samples made using the two E values. The two low magnification micrographs on the left have included the surface scan layer, and three track boundaries (TBs) have been traced and outlined. In the two higher magnification micrographs on the right, TBs can be seen more clearly. As pointed to in Fig. 1a (left micrograph), LOF defect can readily be seen in the 44  $\text{J}/\text{mm}^3$  sample. LOF results from the lack of tracks overlapping. Using ImageJ,  $f_{\text{LOF}}$  has been determined to be 0.5%, which is close to but not fully dense. This agrees with Biffi et al.'s data [7] that at E values of  $\sim 44 \text{ J}/\text{mm}^3$  LPBF samples are not yet fully dense but close to the maximum relative density condition. An increase in E value from 44 to 85  $\text{J}/\text{mm}^3$  in the present work

has resulted in  $f_{\text{LOF}} = 0$ . But, in the 85  $\text{J}/\text{mm}^3$ -sample micrograph, keyhole pores can be seen, as shown in Fig. 1b (right micrograph). Using ImageJ,  $f_{\text{Pores}}$  have been detected to be 0.47%. It can thus be suggested that the E values of 55–65  $\text{J}/\text{mm}^3$  can be used for basically LOF and pore defect-free LPBF.

The left traced tracks in left micrographs of Fig. 1 have been indicated in full by using the traced portion on the right side to add to the other side, and this added portion is indicated by the dotted line. The track width ( $W_{\text{Tr}}$ ) can be estimated based on all the five tracks (two not outlined). The track penetration depth ( $d_p$ ) can be measured. The values of  $W_{\text{Tr}}$ ,  $d_p$ , and  $W_{\text{Tr}}/d_p$  are listed in Table 1. The cross-sectional area ( $A_{\text{Tr}}$ ) of a track can also be estimated using ImageJ, and values are also listed in Table 1, where  $W_{\text{Tr}}$  and  $A_{\text{Tr}}$  have been corrected for the track cross sections being not normal ( $\sim 10^\circ$ ) to the scan direction. Increasing P (thus E as v did not change) has increased both  $W_{\text{Tr}}$  and  $d_p$ , but the increase in  $d_p$  is more profound; thus  $W_{\text{Tr}}/d_p$  has decreased from 2.5 to 2.0. A further feature is the angle ( $\alpha$ ) shown in Fig. 1a (left micrograph) between the tangent at the end of a TB and BD. For the 44  $\text{J}/\text{mm}^3$ -sample,  $\alpha \approx 22^\circ$ . For the 85  $\text{J}/\text{mm}^3$ -sample, as can be suggested by observing the TBs outlined in Fig. 1b (left micrograph),  $\alpha \approx 0^\circ$ . This may be the result that, given the same laser spot size, increasing P increases the energy for melting more vertically than laterally, thus decreasing both  $\alpha$  and  $W_{\text{Tr}}/d_p$ . The increase in E by 93% (from 44 to 85  $\text{J}/\text{mm}^3$ ) has resulted in an increase of  $A_{\text{Tr}}$  (from 4446 to 7444  $\mu\text{m}^2$ ) and thus melt volume by 67%.

The surface appearance of the two samples is shown in Fig. 2, where “ripples” and surface TBs can be seen. A “ripple” is the melt pool boundary on the surface at a time during LPBF. Each arrow in Fig. 2 points to the scan direction of the track, and the arrow has been drawn along the TB, although for the 44  $\text{J}/\text{mm}^3$ -sample, TBs are slightly wavy. A complete melt pool cannot be traced, as a large part of a solidified pool boundary (“ripple”) has been melted in the following track scan, but a part of the melt pool “ripple” can be traced. In Fig. 2, a dotted line represents the trace of a “ripple”. The area bound by an arrowed line and a dotted line represents a part of the melt pool behind the laser spot at a time during LPBF. Comparing the two images, it can generally be suggested that, on average, the angle ( $\beta$ ), as one labelled in Fig. 2a, between the “ripple” trace tail and TB appears to be higher in the 44  $\text{J}/\text{mm}^3$ -sample than in the 85  $\text{J}/\text{mm}^3$ -sample. This may suggest that the melt pool is more elongated in the 85  $\text{J}/\text{mm}^3$ -sample than in the 44  $\text{J}/\text{mm}^3$ -sample. A longer melt track with the higher E condition should suggest a higher melt temperature.

### 3.2. Laser power/energy, Ni content and crystal structure

Estimation of Ni content of the Nitinol powder using EDS is illustrated in Fig. 3. Area EDS of 21 particles (Fig. 3a) were analyzed. A typical EDS spectrum in Fig. 3b shows the Ni and Ti peaks based on which Ni content was determined. The Ni peaks are far apart from Ti peaks, and the intensities of the peaks are strong, providing a sound base for the analysis and calculation of the composition. Based on the analysis of 21 particles,  $\text{at}\% \text{Ni} = 50.47$ , with standard deviation being ( $\text{SD} =$ )  $\pm 0.17\text{at}\%$  and standard error being ( $\text{SE} =$ )  $\pm 0.04\text{at}\%$ . With the low SE value, it may be suggested that the value of Ni content one digit after the decimal point is highly certain. In the following, when values of Ni content are presented, the second digit after the decimal point is kept.

For LPBF samples, analysis was first conducted to detect if Ni content may be location dependent within a track. An example is illustrated in Fig. 4 with the data listed in Table 2 using the 44  $\text{J}/\text{mm}^3$ -sample. There are 7 locations next to and along TB and another 7 locations inside and away from TB where Ni contents have been determined. The mean, SD, and SE values have been calculated and included in Table 2. Clearly, Ni content of location next to

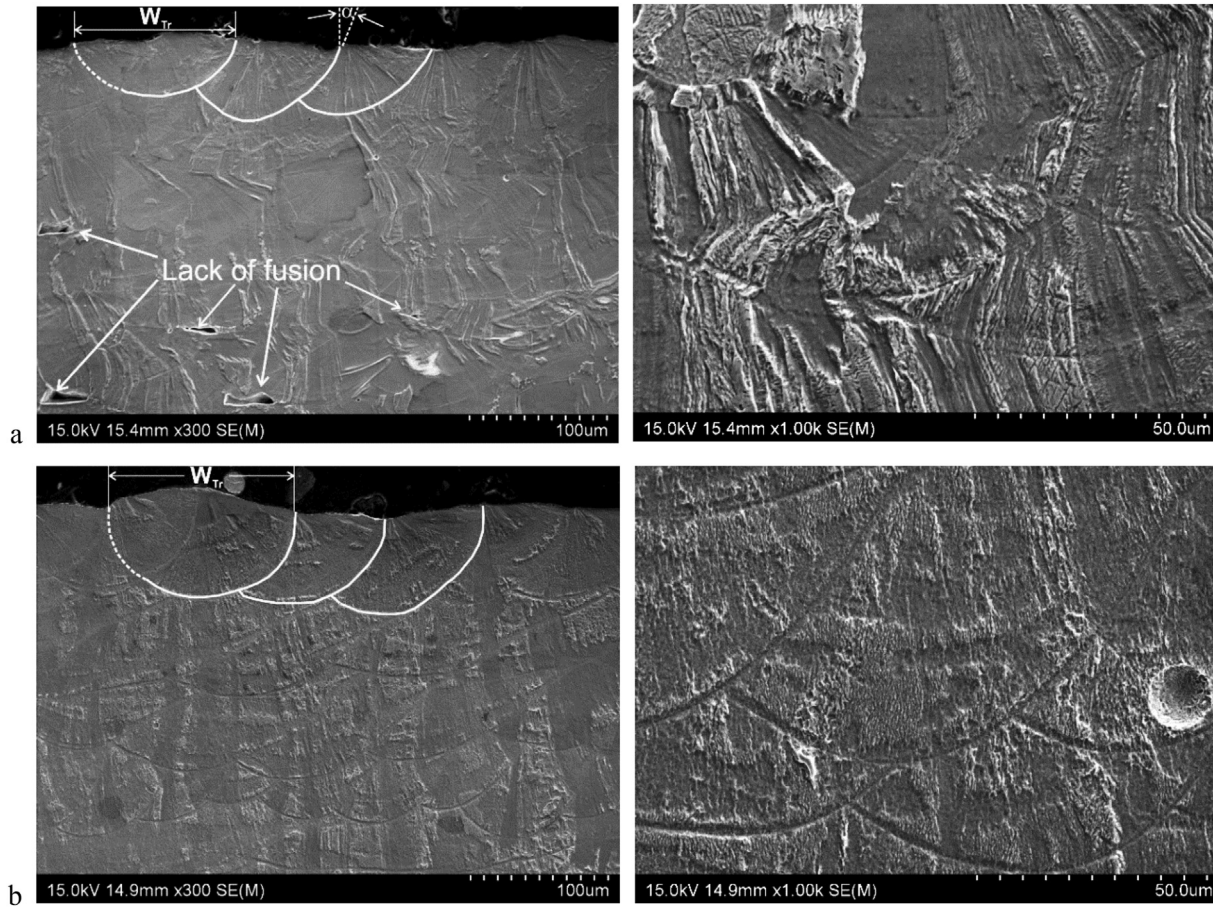


**Fig. 1.** SEM micrographs (left - low magnification, including the surface scan layer with three tracks outlined and right - higher magnification displaying track boundaries clearer): (a) 44 J/mm<sup>3</sup> and (b) 85 J/mm<sup>3</sup>. Note: a number of LOFs are pointed to in the left micrograph of (a) and a keyhole pore is present in the right micrograph of (b).

**Table 1**

Values of track width, penetration depth, width/penetration ratio, track cross sectional area and width/area ratio for the two LPBF samples. Note: Errors are standard deviations.

Sample	$W_{Tr}$ , $\mu\text{m}$	$d_p$ , $\mu\text{m}$	$W_{Tr}/d_p$	$A_{Tr}$ , $\mu\text{m}^2$	$W_{Tr}/A_{Tr}$
44 J/mm <sup>3</sup>	$122 \pm 8$	$49 \pm 6$	2.5	$4446 \pm 490$	0.027
85 J/mm <sup>3</sup>	$141 \pm 5$	$65 \pm 5$	2.0	$7444 \pm 538$	0.019

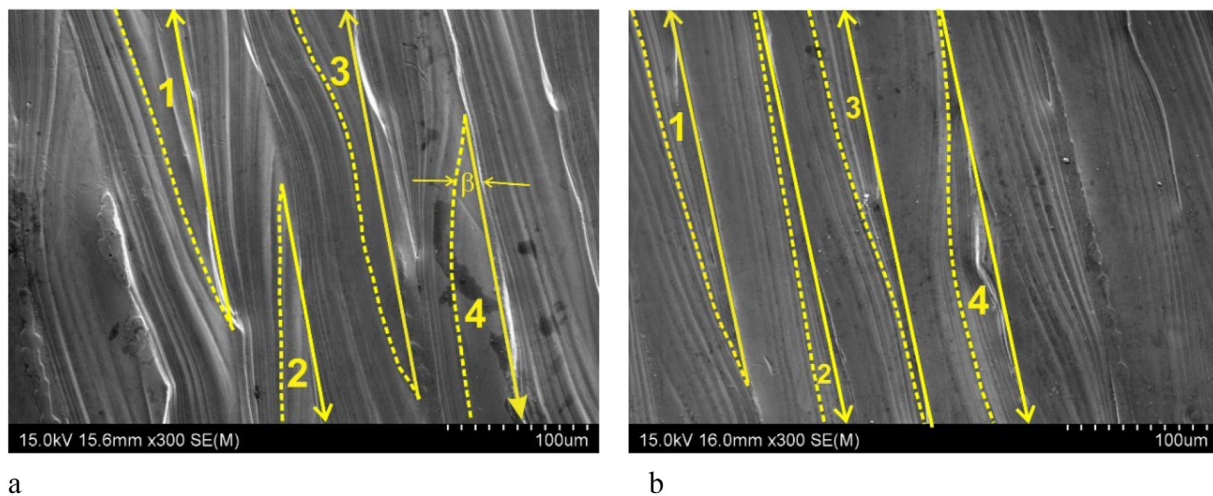


**Fig. 2.** SEM images of sample surfaces: (a) 44 J/mm<sup>3</sup> and (b) 85 J/mm<sup>3</sup> samples. Arrows point to scan direction along the track boundaries. For each arrow the shape of the area bounded by the arrow and dotted line indicates the partial melt pool at a time.

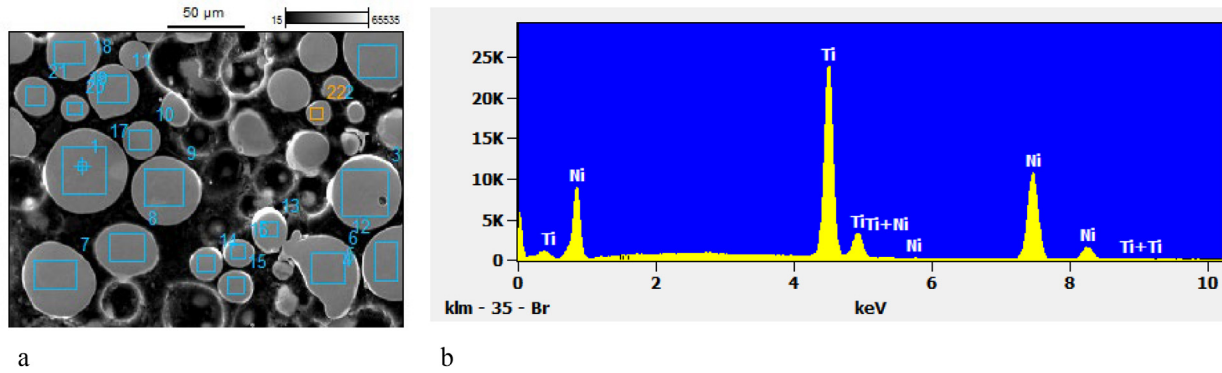


Fig. 3. EDS analysis of powder: (a) SEM image of powder showing area EDS in each powder and (b) a typical spectrum showing the Ti and Ni peaks.

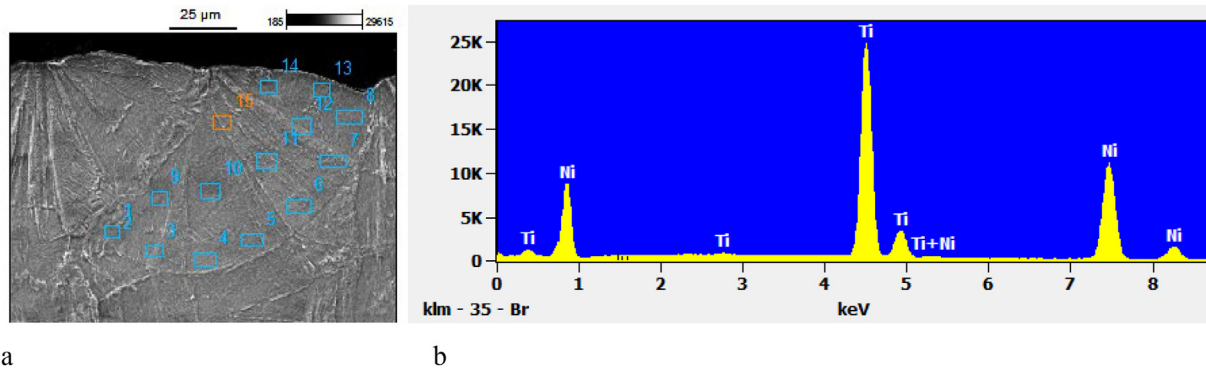


Fig. 4. EDS analysis of the 44 J/mm<sup>3</sup> sample: (a) SEM image illustrating the EDS areas in various locations in a track, 7 next to and along the track boundary (TB) and 7 inside the track, and (b) a typical spectrum showing the Ti and Ni peaks.

Table 2

Ni content in at% (mean SD and SE) in various EDS locations shown in Fig. 4a, next to TB (1st row) and inside the track (2nd row).

Next to TB	50.23	50.00	50.11	50.05	50.10	50.21	50.16	Mean = <b>50.12</b>	SD = 0.08	SE = 0.03
Inside track	50.03	50.08	50.11	50.04	50.22	50.21	50.06	Mean = <b>50.11</b>	SD = 0.08	SE = 0.03

and along TB is the same as Ni content inside and away from TB. The temperature of TB (liquidus 1310 °C and solidus 1240 °C for Nitinol) is lower than the temperatures inside the track and particularly lower than the temperature of the mid-surface location of the track, which could be up to the boiling point (2730 °C for Ni). The lack of difference in Ni content between that near TB and that inside the track is likely the result of the melt being highly convective within the melt pool during its melt time.

Data in Table 3 show that the Ni content of the 44 J/mm<sup>3</sup>-sample is (50.47at%-50.11at%=) 0.36at% lower than the Ni content of the powder. EDS analysis data points are 21 for the powder sample and 14 for the 44 J/mm<sup>3</sup>-sample. That SD values are not high and SE values are low has provided a high confidence for the mean values. Further to the EDS analysis of powder and the low E (44 J/mm<sup>3</sup>) sample, analysis was conducted in the 85 J/mm<sup>3</sup>-sample,

similarly to that for the low E sample. Table 3 lists the values of mean, SD, and SE for the powder and the two LPBF samples for comparison and shows the Ni loss ( $\Delta\text{at}\%\text{Ni}$ ) due to LPBF. An increase in E from 44 to 85 J/mm<sup>3</sup> has resulted in a significantly higher Ni loss at 0.56at% (=50.47at%-49.85at%).

During LPBF, heating is regarded as conduction mode if E and the vaporisation rate are not high. At a sufficiently high E value, a narrowly focussed energy source induced keyhole forms, which relies on the material's evaporation and results in a deep penetration pool. Conduction mode is suggested to be dominant when  $W_{\text{Tr}}/d_p$  is 2 or higher [9,10]. Otherwise, keyhole mode is dominant. For the 44 J/mm<sup>3</sup>-sample,  $W_{\text{Tr}}/d_p = 2.5$ ; thus, melting is in conduction mode. For the 85 J/mm<sup>3</sup>-sample,  $W_{\text{Tr}}/d_p = 2.0$ , a small degree of keyhole melting may be the case, and thus a small amount of keyhole pores has been detected. As presented and explained, in

Table 3

Ni contents (mean, standard deviation, and standard error) values in at% of powder and samples made using the two LPBF conditions.

	Mean	SD	SE	$\Delta\text{Ni}$
Powder	50.47	±0.17	±0.04	
E = 44 J/mm <sup>3</sup>	50.11	±0.08	±0.02	0.36
E = 85 J/mm <sup>3</sup>	49.91	±0.14	±0.02	0.56

**Table 1**, the increase of 93% in E has increased the volume of melt by 67%. However, the increase in Ni loss was 56%,  $= (0.56 - 0.36) / 0.36$ . In other words, a 67% increase in melt volume has resulted in a 55% increase in Ni loss. As shown in **Table 1**, increasing E has increased  $W_{Tr}$  but has reduced  $W_{Tr}/A_{Tr}$  from 0.027 to 0.019. A relatively less melt surface (per unit volume of melt) may have contributed to a less amount of Ni in the melt to vaporize through the melt surface, despite of the melt temperature being higher with a small degree of keyhole mode melting for the higher E LPBF.

How Ni loss may have affected the structure at room temperature has been studied using XRD analysis. XRD patterns for the powder and the two LPBF samples are shown in **Fig. 5**. In the powder pattern, there are three diffraction peaks, at  $2\theta = 42.4^\circ$ ,  $61.5^\circ$  and  $77.6^\circ$ . According to JCPDS file 18-899 [8] for B2 NiTi,  $a = 0.2998$  nm and the first three main diffraction peaks are from 110, 200 and 211. As  $\lambda = 0.154$  nm, these diffraction peaks should be at  $42.59^\circ$ ,  $61.81^\circ$  and  $77.96^\circ$ , very close to the  $2\theta$  values of the peaks detected in the powder pattern in **Fig. 5**. Thus, the powder is fully B2 structure, although normalised intensity ( $I/I_0$ ) value is 100 for 110, 9 for 200 and 13 for 211, while in the JCPDS file  $I/I_0$  is 100, 40 and 60, respectively [8]. In the powder XRD patterns using  $\lambda = 0.154$  nm and having the same three peaks and no other diffraction peaks for  $2\theta$  up to  $80^\circ$  from a number of Nitinol LPBF studies [11–13], with Ni content from 50.3 to 50.8at%, similar  $I/I_0$  values to the values in the powder pattern in **Fig. 5** are shown.

In the  $44 \text{ J/mm}^3$ -sample pattern, the three main diffraction peaks (110, 200, and 211) of the B2 phase have clearly appeared (red in **Fig. 5**). Compared to the powder pattern, peak intensities for the LPBF ( $44 \text{ J/mm}^3$ ) sample are considerably lower. This is due mainly to the small size of the LPBF sample used for XRD, but also, the structure is not fully B2. A small diffraction peak at ( $2\theta =$ )  $39.6^\circ$  can be detected, corresponding to  $d = 0.227$  nm. The peak can be attributed to the diffraction from (020) of B19', which is the second most intensive diffraction peak for B19' (at  $39.2^\circ$ ) in powder diffraction, according to JCPDS file 35-1281 [8]. The JCPDS file also lists an equal second most intensive peak, which is 002 at  $43.9^\circ$ . The more intensive diffraction (powder diffraction) peak for B19' should be 111 at  $44.9^\circ$  and also  $11\bar{1}$  at  $41.4^\circ$  for B19'.

In the powder XRD pattern, as shown in **Fig. 5b**, the intensity value for  $110_{B2}$  reduces to about the background (noise) level meaning that  $I = 0$  for  $2\theta$  being  $\pm 0.6^\circ$  outside of the  $2\theta (=42.5^\circ)$  of the  $110_{B2}$  peak and that there is little  $110_{B2}$  for  $2\theta$  less than  $41.9^\circ$

and  $2\theta > 43.1^\circ$ . But for the  $44 \text{ J/mm}^3$ -sample, on the left side of the  $110_{B2}$  peak, the intensity has not dropped to zero (background level) between  $39.6^\circ$  (the  $020_{B19'}$  peak) and  $41.6^\circ$ . On the right side, the intensity has not dropped to zero after  $42.8^\circ$  until after  $45.5^\circ$ . This is despite of the considerably smaller diffraction peaks for B2 in the  $44 \text{ J/mm}^3$ -sample, due to the small XRD sample size, than the peaks of the powder sample.  $11\bar{1}_{B19'}$ , at  $41.4^\circ$  for B19' on the left side of the  $110_{B2}$  peak and  $111_{B19'}$  at  $44.9^\circ$  on the right side of  $110_{B2}$  peak have thus contributed to the higher than zero intensity values for  $2\theta$  ranged at  $39.6^\circ$ – $41.6^\circ$  and at  $42.8^\circ$ – $45.5^\circ$ . Thus, a small amount of B19' phase is present in the  $44 \text{ J/mm}^3$ -sample.

In the  $85 \text{ J/mm}^3$ -sample pattern (blue in **Fig. 5**), a small amount of B19' phase being present can also be suggested. This is based on the low intensity peaks of  $020_{B19'}$  and  $111_{B19'}$ , as well as the non-zero intensity at ( $2\theta =$ )  $41.4^\circ$  for 111 and at  $43.9^\circ$  for 002 in the pattern, similar to those present in the  $44 \text{ J/mm}^3$ -sample pattern, which have already been explained. However, diffraction peaks for B2 in the  $85 \text{ J/mm}^3$ -sample differ in intensities from those in the  $44 \text{ J/mm}^3$ -sample. For  $110_{B2}$  in the  $85 \text{ J/mm}^3$ -sample pattern, the intensity is about twice as strong as that in the  $44 \text{ J/mm}^3$ -sample pattern. After normalising,  $I/I_0$  for  $200_{B2}$  in the  $85 \text{ J/mm}^3$ -sample pattern is  $\sim 80\%$  higher than  $I/I_0$  for  $200_{B2}$  in the  $44 \text{ J/mm}^3$ -sample pattern. On the other hand, no  $211_{B2}$  is detected in the  $85 \text{ J/mm}^3$ -sample pattern. In the pattern with XRD conducted on the surface parallel to BD of Nitinol LPBF sample [14],  $211_{B2}$  peak intensity is close to zero. On the other hand, in the pattern with XRD conducted on the sample surface normal to BD of Nitinol LPBF sample produced using electron beam PBF [15],  $211_{B2}$  is absent. The absence of the  $211_{B2}$  peak in the pattern of  $85 \text{ J/mm}^3$  sample may have resulted from the possible double textures of 110 and 200 in the plane parallel BD.

The above structure analysis has suggested that, using E values ranged from  $44$  to  $85 \text{ J/mm}^3$ , LPBF of Nitinol with the current starting composition of 50.5at%Ni has only affected the structure slightly. This is in spite of the loss of Ni being 0.56at% at the high E value of the E range. The structure of the samples remaining largely austenitic suggests that defect-free LPBF of Nitinol with a suitable starting Ni content is suitable for manufacturing of stents. This is because that, as has been explained in Introduction, the structure of Nitinol stents at room temperature needs to be austenitic for the  $A \rightarrow M$  induced superelasticity required for stenting to be realised.

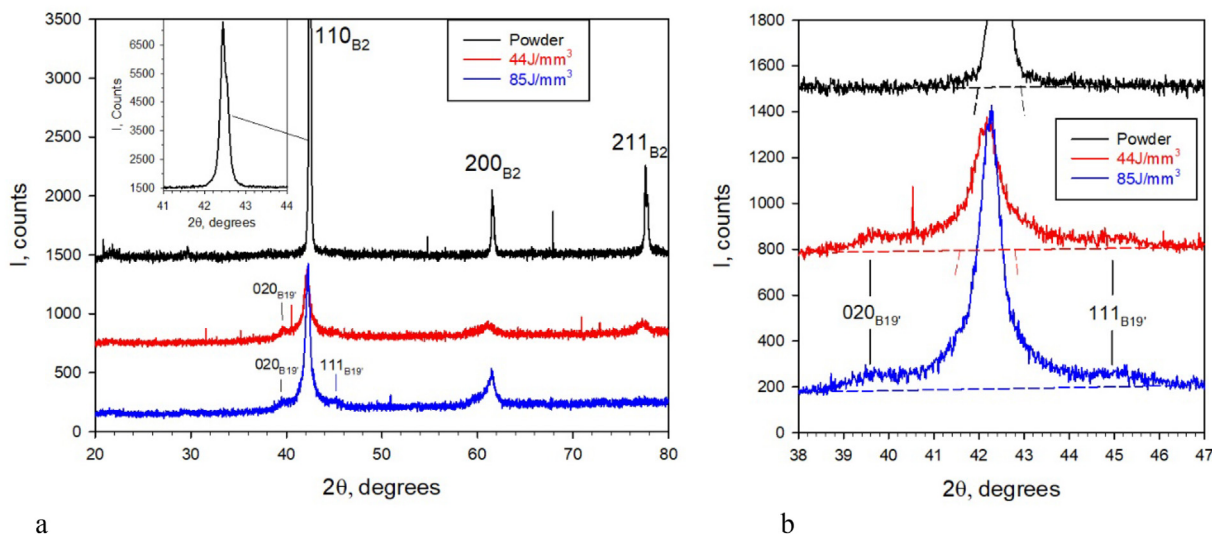


**Fig. 5.** X-ray diffraction patterns of powder,  $44 \text{ J/mm}^3$  and  $85 \text{ J/mm}^3$  samples: (a) pattern for  $2\theta$  from 20 to  $80^\circ$  with main diffraction peaks from B2 and weak diffraction peaks from B19' indicated, and (b)  $2\theta$  from 38 to  $47^\circ$  with background base lines indicated.

#### 4. Conclusions

Using a low laser power but close to fully dense LPBF condition ( $E = 44 \text{ J/mm}^3$ ), 0.36at%Ni loss has been found. Using a sufficiently high  $E$  ( $85 \text{ J/mm}^3$ ) condition so that keyhole pores have formed, the loss of Ni has been detected to be 0.56at%. Thus, for defect-free LPBF, 0.4–0.5at%Ni loss is expected. The higher (93%)  $E$  condition has resulted in a 67% increase in the amount of melting, but due to laser spot size being constant, the depth of the melt has increased more than the increase in width. This is consistent with the determined ratio of the surface area over the volume of the melt having reduced from 2.7 to 1.9 with the increase in  $E$  from 44 to  $85 \text{ J/mm}^3$ . Thus, Ni loss is 55% higher rather than 67% higher when  $E$  has increased 93% to result in the increase in melt volume by 67%, despite of the increase in  $E$  having caused the start of vaporization induced keyhole melting mode. With the powder containing 50.5at%Ni detected by SEM/EDS and being fully austenitic, the LPBF as-built structure has remained largely austenitic, although the presence of martensite phase has been detected. The XRD data have suggested double preferred growth orientations (200) and (110) during the sufficiently high  $E$  LPBF.

#### CRedit authorship contribution statement

**E.M. Sequeda Leon:** Investigation, Methodology, Formal analysis, Writing - original draft & review. **S. Singamneni:** Methodology, Resources, Supervision. **T. Guraya:** Formal analysis, Investigation, Methodology. **Z.W. Chen:** Conceptualization, Methodology, Formal analysis, Supervision, Writing – original draft, Writing - review & editing.

#### Data availability

No data was used for the research described in the article.

#### Declaration of Competing Interest

The authors declare that they have no known competing financial interests or personal relationships that could have appeared to influence the work reported in this paper.

#### References

- [1] T.W. Duerig, D.E. Tolomeo, M. Wholey, An overview of superelastic stent design, *Minim. Invasive Ther. Allied Technol.* 2000 (9) (2000) 235–246.
- [2] J. Frenzel, E.P. George, A. Dlouhy, C.h. Somsen, M.-F.-X. Wagner, G. Eggeler, Influence of Ni on martensitic phase transformations in NiTi shape memory alloys, *Acta Mater.* 2010 (58) (2010) 3444–3458.
- [3] T. DebRoy, H.L. Wei, J.S. Zuback, T. Mukherjee, J.W. Elmer, J.O. Milewski, A.M. Beese, A. Wilson-Hid, A. De, W. Zhang, Additive manufacturing of metallic components - process, structure and properties, *Prog. Mater. Sci.* 92 (2018) 112–224.
- [4] I.M. Kusoglu, B. Gökce, S. Barcikowski, Research trends in laser powder bed fusion of Al alloys within the last decade, *Addit. Manuf.* 36 (2020).
- [5] Z. Wu, S.P. Narra, A. Rollett, Exploring the fabrication limits of thin-wall structures in a laser powder bed fusion process, *Int. J. Adv. Manuf. Technol.* 110 (2020) 191–207.
- [6] O.A. Mohamed, S.H. Masood, W. Xu, Nickel-titanium shape memory alloys made by selective laser melting: a review on process optimisation, *Adv. Manuf.* 10 (2022) 24–58.
- [7] C.A. Biffi, J. Fiocchi, F. Valenza, P. Bassani, A. Tuissi, Selective laser melting of NiTi shape memory alloy: Processability, microstructure, and superelasticity, *Shape Memory Superelast.* 6 (2020) 342–353.
- [8] Joint Committee on Powder Diffraction Standards (JCPDS), *Powder Diffraction File-Inorganic Vol.*, International Centre for Diffraction Data, Swarthmore, NJ, 1997.
- [9] W.E. King, H.D. Barth, V.M. Castillo, G.F. Gallegos, J.W. Gibbs, D.E. Hahn, C. Kamath, A.M. Rubenchik, Observation of keyhole-mode laser melting in laser powder-bed fusion additive manufacturing, *J. Mater. Process. Technol.* 214 (2014) 2915–2925.
- [10] A.M. Rubenchik, W.E. King, S.S. Wu, Scaling laws for the additive manufacturing, *J. Mater. Process. Technol.* 257 (2018) 234–243.
- [11] W. Chen, Q. Yang, S. Huang, S. Huang, J.J. Krusic, X. Li, Laser power modulated microstructure evolution, phase transformation and mechanical properties in NiTi fabricated by laser powder bed fusion, *J. Alloy. Compd.* 861 (2021).
- [12] A. Safdel, M.A. Elbestawi, New insights on the laser powder bed fusion processing of a NiTi alloy and the role of dynamic restoration mechanisms, *J. Alloy. Compd.* 885 (2021).
- [13] K. Khanlari, Q. Shi, X. Yan, K. Hu, C. Tan, P. Kelly, W. Zhang, P. Cao, X. Wang, X. Liu, Printing of NiTiInol parts with characteristics respecting the general microstructural, compositional and mechanical requirements of bone replacement implants, *Mater. Sci. Eng. A* 839 (2022).
- [14] L. Xue, K.C. Atli, C. Zhang, N. Hite, A. Srivastava, A.C. Leff, A.A. Wilson, D.J. Sharar, A. Elwany, R. Arroyave, I. Karaman, Laser powder bed fusion of defect-free NiTi shape memory alloy parts with superior tensile superelasticity, *Acta Mater.* 229 (2022).
- [15] Q. Zhou, M.D. Hayat, G. Chen, S. Caid, X. Qu, H. Tang, P. Cao, Selective electron beam melting of NiTi: Microstructure, phase transformation and mechanical properties, *Mater. Sci. Eng. A* 744 (2019) 290–298.